

Magnetic order and magneto-transport in half-metallic ferrimagnetic $\text{Mn}_y\text{Ru}_x\text{Ga}$ thin films

K.E. Siewierska,^{1,*} G. Atcheson,¹ A. Jha,¹ K. Esien,² R. Smith,¹ S. Lenne,¹
N. Teichert,¹ J. O'Brien,¹ J.M.D. Coey,¹ P. Stamenov,¹ and K. Rode¹

¹*School of Physics and CRANN, Trinity College Dublin, Ireland*

²*Queen's University Belfast, Northern Ireland, United Kingdom*

The ruthenium content of half-metallic $\text{Mn}_2\text{Ru}_x\text{Ga}$ thin films, with a biaxially-strained inverse Heusler structure, controls the ferrimagnetism that determines their magnetic and electronic properties. An extensive study of $\text{Mn}_y\text{Ru}_x\text{Ga}$ films on MgO (100) substrates with $1.8 \leq y \leq 2.6$ and $x = 0.5, 0.7$ or 0.9 , including crystallographic, magnetic order, magneto-transport and spin polarisation is undertaken to map specific composition-dependent properties in this versatile ternary system. A comparison of experimental densities obtained from X-ray reflectivity with calculated densities indicates full site occupancy for all compositions, which implies chemical disorder. All moments lie on the Slater-Pauling plot with slope 1 and all except $x = 0.5, y = 2.2$ exhibit magnetic compensation at T_{comp} below 500 K. The coercivity near T_{comp} exceeds 10 T. Increasing the Mn or Ru content raises T_{comp} , but increasing Ru also decreases the spin polarisation determined by point contact Andreev reflection. Molecular field theory is used to model the temperature dependence of the net ferrimagnetic moment and three principal exchange coefficients are deduced. Marked differences in the shape of anomalous Hall and net magnetisation hysteresis loops are explained by substantial canting of the small net moment by up to 40° relative to the c -axis in zero field, which is a result of slight non-collinearity of the Mn^{4c} sublattice moments due to competing intra-sublattice exchange interactions arising from antisite disorder and excess Mn in the unit cell. Consequences are reduced spin polarisation and an enhanced intrinsic contribution to the anomalous Hall effect. The systematic investigation of the physical properties as a function of x and y will guide the selection of compositions to meet the requirements for magnonic and spintronic MRG-based devices.

I. INTRODUCTION

Zero-moment ferrimagnetic half-metals (ZMHM) are attractive materials for applications in spintronic devices. [1, 2] They offer advantages over their antiferromagnetic or half-metallic ferromagnetic counterparts. [3] After their theoretical prediction in 1995[4], various candidate ZMHM materials were proposed over the years based on DFT calculations, including C1_b , CrMnSb , L2_1 , Fe_2VGa and D0_3 Mn_3Ga [5–7]. Unfortunately, the predicted alloys either crystallised in a different structure with no spin gap like Mn_3Ga [8], decomposed into a mixture of simpler phases like CrMnSb or were found to be either nonmagnetic or very weak ferromagnets, like Fe_2VGa [9]. It seemed there might be some reason why the ZMHM was so elusive [6], The first material to show evidence of the long-sought magnetic behaviour was $\text{Mn}_2\text{Ru}_{0.5}\text{Ga}$. [10] Extrapolating between a half-Heusler Mn_2Ga and a full-Heusler Mn_2RuGa , $\text{Mn}_2\text{Ru}_{0.5}\text{Ga}$ was thought to have 21 valence electrons with vacancies on half the Ru^{4d} sites, as shown in Fig. 1. [10] Since its discovery, a few other members of ZMHM material class have been demonstrated, including thin film Mn_3Al [11] and bulk $\text{Mn}_{1.5}\text{V}_{0.5}\text{FeAl}$ [12]. The $\text{Mn}_2\text{Ru}_x\text{Ga}$ (MRG) thin films grown on MgO (001) substrates, where the cubic structure of the inverse Heusler alloy is distorted by biaxial strain, offer perpendicular magnetic anisotropy (PMA) that allows efficient detection and manipulation of the magnetic state. Cubic MRG would crystallise in the $F\bar{4}3m$ (216) space group, with 4 formula units (f.u.) per unit cell, which is adopted when referring to crystallographic vectors and positions, but the symmetry is reduced to $I4m2$ (119) by the

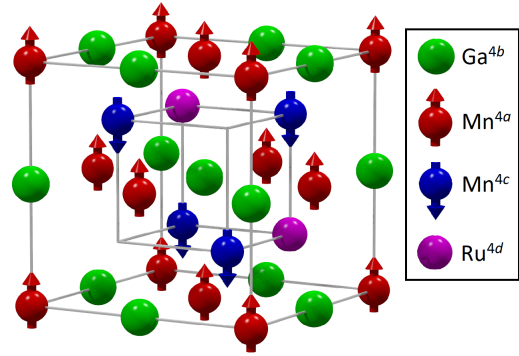


FIG. 1. Model of the inverse Heusler XA structure of $\text{Mn}_2\text{Ru}_{0.5}\text{Ga}$.

tetragonal distortion. In the ideal inverse XA Heusler structure, $4a$ and $4b$ sites are occupied by Mn and Ga, respectively, whereas $4c$ and $4d$ sites are fully occupied by Mn and Ru. [10] Transport and magneto-optic properties are dominated by the Mn^{4c} sublattice because there are few, if any, Mn^{4a} states at the Fermi level. [1, 10, 13] The two manganese sublattice magnetic moments cancel at the compensation temperature T_{comp} . Nevertheless, magnetic domains can be observed by the magneto-optic Kerr effect (MOKE) even at temperatures where there is little or no net magnetisation. [14, 15] As the net moment tends to zero, the anisotropy field becomes large, resulting in high-frequency spin dynamics with low Gilbert damping. [1, 10] A maximum zero-field resonance frequency of ≈ 160 GHz and a Gilbert damping constant $\alpha \approx 0.02$ have been reported. [1, 16]

Remarkably efficient charge/spin conversion and large spin-orbit fields per current density $\frac{\mu_0 H_{\text{eff}}}{j}$ related to spin currents have recently been measured in single thin films of

* siewierk@tcd.ie

MRG, where $\frac{\mu_0 H_{\text{eff}}}{j}$ approaches $0.1 \times 10^{-10} \text{ T/Am}^{-2}$ in the low-current density limit. This is almost a thousand times the Ørsted field and one to two orders of magnitude greater than $\frac{\mu_0 H_{\text{eff}}}{j}$ in heavy metal/ferromagnet bilayers. [17] The efficiency of current induced spin-orbit torque switching in Ru/MRG/MgO has been found to be similar to that of a ferromagnet, e.g. Ta/CoFeB/MgO [18] or Pt/Co/AIO_x [19], despite larger MRG film thickness and coercivity [20]. Furthermore, thermal single-pulse all-optical toggle switching at ultra short timescales ($< 10 \text{ ps}$) has been recently demonstrated in MRG, making it the first non-Gd based material to exhibit this effect. [21–23] MRG-based devices could offer a practical solution to the current problem of chip-to-chip generation and detection of electromagnetic radiation in the 0.1 THz - 10 THz frequency range, known as the ‘THz gap’, provided sufficiently high magnetoresistive effects can be achieved. [1, 24]

Each spintronic application requires a specific set of material properties. For example, efficient single-pulse all optical toggle switching (SPAOS) at room temperature (RT) in MRG films requires T_{comp} to be just above RT. [21] High spin polarisation and perfectly crystalline films with smooth surfaces are desirable for MRG-based magnetic tunnel junctions. Earlier studies have investigated the variation of some of these properties with x in Mn₂Ru_xGa. [10, 13, 25, 26] The results show that an increase in Ru content increases tetragonal distortion of the cubic unit cell on MgO and improves the wetting of the film. These qualities are useful for all applications, and particularly for the fabrication of nanostructured devices. [13, 25]

The goal of the present work is to help identify compositions which exhibit the best combinations of properties for specific applications. Thin thin films are prepared with varying Ru and Mn content, while keeping the Ga content fixed. The dominant contribution of Mn^{4c} sites to the density of states at the Fermi level allows us to disentangle net and sublattice magnetisations with the aim of establishing non-collinearity of the Mn^{4c} sublattice moments, which results in the canting of net moment.

II. METHODOLOGY

Epitaxial thin films of Mn_yRu_xGa (MRG) with $x + y \approx 3$ were grown by DC magnetron sputtering on $10 \times 10 \text{ mm}^2$ (100) MgO substrates in our Shamrock sputtering system [1, 10]. The base pressure of the system was 10^{-8} Torr . Films were co-sputtered in argon onto single-side polished substrates maintained at $350 \text{ }^\circ\text{C}$ from three 75 mm targets of Mn₂Ga, Ru and either MnGa or Mn₃Ga. Deposition rates from each target were calibrated and used to determine the values of x and y in the formula. Films were capped in-situ with a 3 nm layer of AlO_x deposited at room temperature to prevent further oxidation. Film thickness and rms roughness were determined by low-angle X-ray scattering in a Panalytical X’Pert Pro diffractometer, and thickness was found by fitting the interference pattern using X’Pert Reflectivity Software. A Bruker D8 Discovery X-ray diffractometer with a copper tube (K_α wavelength = 154.06 pm) and a double-bounce Ge [220] monochromator on the primary beam was

used to determine the diffraction patterns of the thin films. Reciprocal space maps were obtained on the same diffractometer around the (113) MgO reflection.

Magnetisation measurements with the field applied perpendicular or parallel to the surface of films mounted in a straw were made using a 5 T Quantum Design SQUID magnetometer. Data included hysteresis loops and thermal scans from 10 K - 400 K. They were corrected for the magnetism of the substrate. Thermal scans in zero field after saturation of the magnetisation at room temperature were used to determine the compensation temperatures of the films. For Kerr imaging, an Evico Magnetics wide-field Kerr microscope with a 10x/0.25 objective lens was used. All loops were measured with polar sensitivity and red LED light with a field applied out-of-plane. Faraday rotation was compensated during the measurement using a feature which readjusts the analyser position relative to a mirror reference.[27] Samples were heated from 300 K - 500 K on a temperature-controlled microscope stage.

Electrical measurements were made in a 1 T GMW electromagnet under ambient conditions. Silver wires were cold-welded to the films with indium and the current used was 5 mA. High field data were obtained in a 14 T Quantum Design Physical Property Measurement System (PPMSTM). The films there were contacted with silver paint. The 4-point Van der Pauw geometry was used to determine both the Hall resistivity and the longitudinal resistivity of the films.

Point contact Andreev reflection (PCAR) measurements were made in the PPMS using a mechanically sharpened Nb tip. Landing the tip onto the sample surface is controlled by an automated vertical Attocube piezo-stepper. Two horizontal AttocubeTM steppers are used to move the sample laterally to probe a pristine area. The differential conductance spectra were fitted using a modified Blonder-Tinkham-Klapwijk model, as detailed elsewhere.[28, 29]

III. RESULTS

Typical small-angle X-ray scattering data shown in Fig. 2a attest to the film quality. Film and cap layer thickness values for all films were $50 \pm 5 \text{ nm}$ and $3 \pm 2 \text{ nm}$, respectively and root mean square roughness were deduced from these data. The films are tetragonally elongated by about 1 % as a result of biaxial compressive strain imposed by the substrate. A typical X-ray diffraction pattern in Fig. 2b shows only the c -axis (002) and (004) reflections as expected from a perfectly textured film. The growth axis corresponds to the crystallographic c -axis. Broadening of the reflections is mainly due to the film thickness.

In order to determine both unit cell parameters, and visualise the strain in the film, reciprocal space maps were recorded around the [113] MgO reflection. An example is shown in Fig. 3. The a -parameter of MRG is constrained by the substrate to be $\sqrt{2}a_{\text{MgO}} = 595 \text{ pm}$, whereas the c -parameter expands by about 1 %.

The densities of the films were obtained from the low angle X-ray reflectivity data. Theoretical densities are calculated from the atomic formulae reduced to exactly four atoms

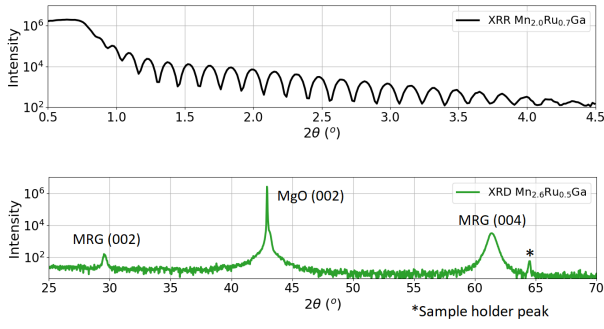


FIG. 2. X-ray analysis of MRG thin films: (a) XRR pattern of $\text{Mn}_{2.0}\text{Ru}_{0.7}\text{Ga}$ and (b) XRD pattern of $\text{Mn}_{2.6}\text{Ru}_{0.5}\text{Ga}$. The peak marked * is due to the sample holder.

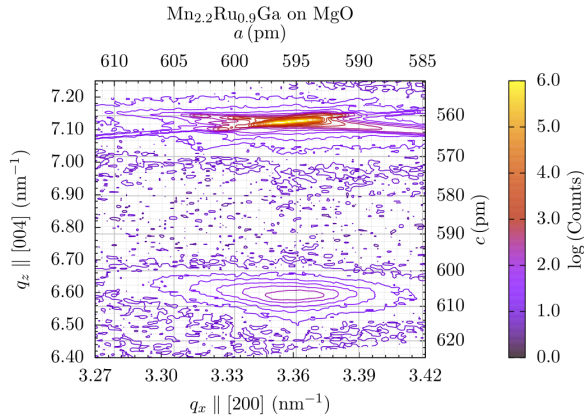


FIG. 3. Reciprocal space map of $\text{Mn}_{2.2}\text{Ru}_{0.9}\text{Ga}$ of MgO (113) and MRG (204) reflections. Lattice parameters are calculated with respect to the MRG unit cell.

per formula unit, using the experimentally determined a - and c -parameters to determine the cell volume. Calculating densities for $\text{Mn}_2\text{Ru}_{0.5}\text{Ga}$, for example, by assuming full occupancy or two vacancies per unit cell unit gives 7900 kg/m^3 or 7100 kg/m^3 , respectively. The density obtained from fitting the XRR pattern was 7800 kg/m^3 . This shows that the vacancy assumption underestimates the density by 9 %, whereas the experimental density agrees with that calculated for full occupancy to within about 1 %. A comparison of experimental and calculated densities of nine films for full occupancy is shown in Fig. 4, where it is seen that the values agree to within 3 %. The densities predicted for the formulae with 0.3 or 0.1 vacancies and 0.1 interstitial Mn atoms are marked by yellow crossed bars. We conclude that all the crystallographic sites in MRG really are close to fully occupied. Overall, the density increases with increasing Ru content as expected. The number of valence electrons n_v per formula unit is included in Table I.

Net magnetisation and hysteresis were measured by SQUID magnetometry. Compensation temperatures were deduced from the change of sign of the remanent magnetisation in zero applied field found from thermal scans, after saturating in 5 T at 400 K. All samples bar one exhibited a compensation point.

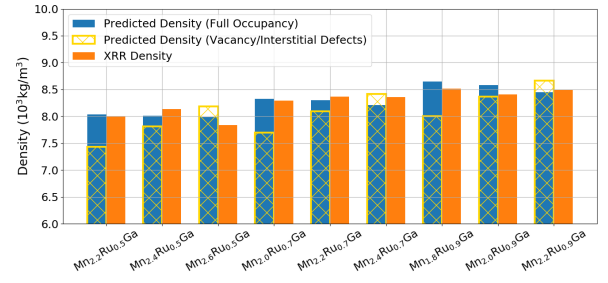


FIG. 4. Calculated (blue) and experimental (orange) densities for the nine MRG films. The yellow crossed bars show densities predicted if there were vacancies/interstitials in the structure.

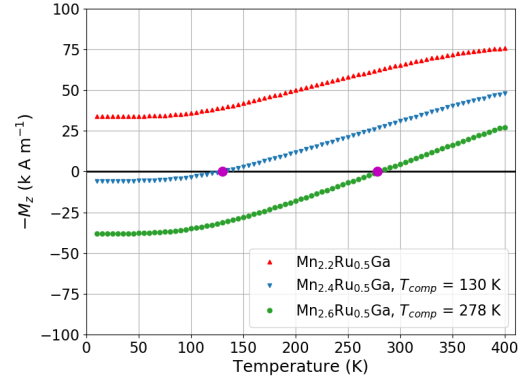


FIG. 5. Temperature scans of the remanence of several MRG films with $x = 0.5$, used to determine the compensation temperature.

Some of the thermal scans are presented in Fig. 5. Curie temperatures were all above 400 K, the temperature limit of our SQUID measurements.

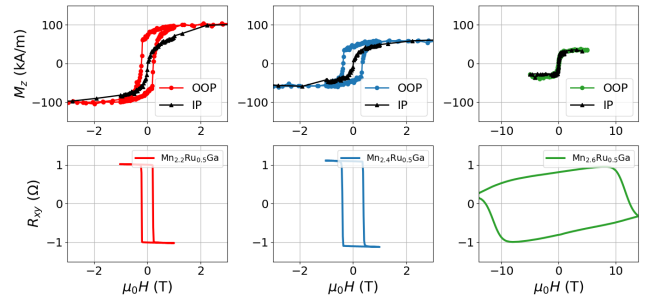


FIG. 6. MRG thin films for the $x = 0.5$ series. Top panel: Magnetisation and curves measured parallel (IP) and perpendicular (OOP) to the film plane. Bottom panel: Corresponding anomalous Hall effect curves. Note the applied field in the third panel on the right ranges from -14 T to +14 T.

Hysteresis in these films can be extremely large close to compensation because the anisotropy field $\mu_0 H_A = 2K_1/M_s$ diverges as the net magnetisation M_s falls to zero. The net magnetisation measured by SQUID magnetometry with the field applied parallel or perpendicular to the film plane is shown for three $x = 0.5$ films in the top panel of Fig. 6. The

coercivity in the out of plane loop agrees with that seen in the anomalous Hall effect (Bottom panel). All in-plane loops exhibit a soft component that saturates in about 50 mT. This behaviour will be discussed in Section V.

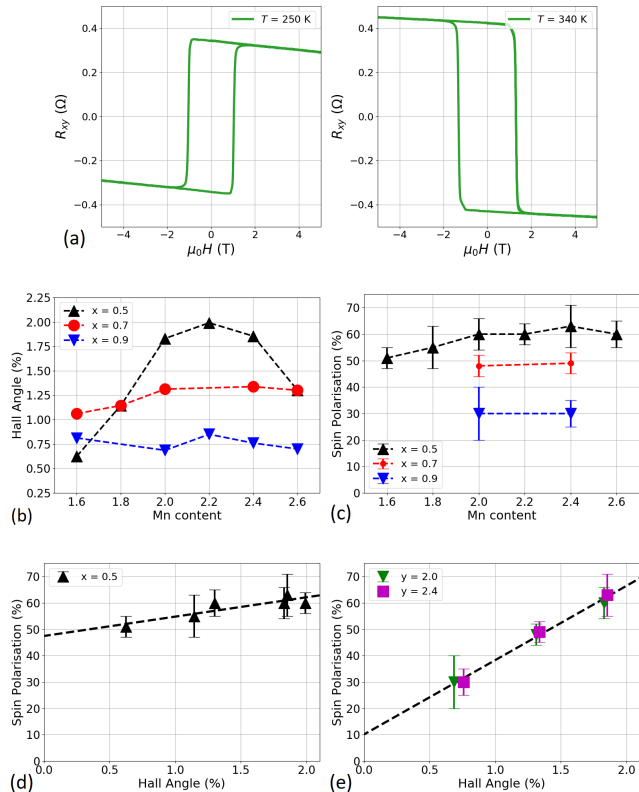


FIG. 7. Anomalous Hall effect: (a) anomalous Hall hysteresis loops for $\text{Mn}_{2.6}\text{Ru}_{0.5}\text{Ga}$ below (250 K), and above (340 K) compensation ($T_{\text{comp}} = 278$ K). (b) Hall angles and (c) spin polarisation for three series in an extended range of Mn composition. The spin polarisation versus anomalous Hall angle for constant (d) $x = 0.5$ and (e) $y = 2.0, 2.4$.

The anomalous Hall effect cannot provide the magnitude of the sublattice magnetisation as it results from spin-dependent scattering and band structure effects [30], but the coercivity is determined accurately, and the dominant sublattice is obvious from the loop shape. Fig. 7a shows the reversal of the Hall loop on crossing compensation. The Hall signal is dominated by the Mn^{4c} sublattice that contributes the majority of states close to the Fermi level. This sublattice is magnetically dominant below, but not above, T_{comp} as can be inferred from the sign of the anomalous Hall coefficient. Sample $\text{Mn}_{2.6}\text{Ru}_{0.5}\text{Ga}$ compensates at 278 K, where the coercivity diverges. The minor loop at room temperature already exhibits a coercivity of 12 T (Fig. 6, bottom right panel). The anomalous Hall angle at room temperature, defined as the ratio of the Hall resistivity at saturation to the longitudinal resistivity reaches a maximum of 2 % for the $x = 0.5$ series when $y = 2.2$, as shown in Fig. 7b. Spin polarisation data determined by point contact Andreev reflection are summarised in Fig. 7c. The $x = 0.5$ series (in black) shows a maximum spin polarisation at the Fermi level of 63 % for $y = 2.4$. Alloys with a higher ruthenium

content have a considerably smaller spin polarisation. The spin polarisation is linearly dependent on the anomalous Hall angle θ_{AH} for $x = 0.5$ and $y = 2.0, 2.4$ as shown in Figs. 7d and 7e, respectively. This demonstrates that the band structure accounts for θ_{AH} , which is dominated by the lowest concentration of carriers and confirms that Mn^{4c} sublattice electrons dominate the transport. A summary of the crystallographic and magnetic properties on the nine MRG films is provided in Table I. All films show compensation, with the exception of $\text{Mn}_{2.2}\text{Ru}_{0.5}\text{Ga}$.

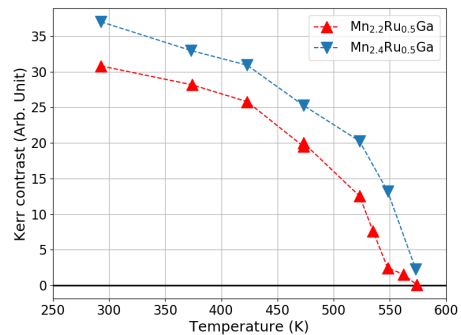


FIG. 8. Temperature dependence of the optically dominant sublattice, measured by MOKE microscopy.

MOKE signal shown in Fig. 8 is essentially that of the Mn^{4c} sublattice magnetisation. The MOKE contrast falls to zero at the ordering temperature, tabulated in Table I. The domain patterns in zero applied field tend to get frozen by defect networks, or whenever the hysteresis exceeds the stray field due to the small net magnetisation. [15]

TABLE I. Compositions, number of valence electrons, crystallographic and magnetic properties of three series of MRG thin films where the Mn and Ru content are varied. M_0 and m_0 are magnetisation and moment at $T = 4$ K, respectively.

Mn, Ru y, x	n_v	c (pm)	a (pm)	ρ (kg/m^3)	M_0 (kA/m)	m_0 ($\mu_B/\text{f.u.}$)	T_{comp} (K)	T_C (K)
2.2, 0.5	24.2	605	597	8003	-33	-0.19	-	550
2.4, 0.5	24.4	604	596	8135	6	0.03	130	577
2.6, 0.5	24.6	604	595	7840	38	0.22	278	592
2.0, 0.7	24.4	605	598	8296	13	0.08	165	530
2.2, 0.7	24.6	605	596	8365	43	0.25	311	543
2.4, 0.7	24.8	606	596	8359	67	0.39	381	494
1.8, 0.9	24.6	608	596	8513	36	0.21	235	478
2.0, 0.9	24.8	606	596	8409	61	0.35	375	513
2.2, 0.9	25.0	607	597	8496	111	0.65	436	491

IV. MEAN FIELD THEORY

Zero-field thermal scans of net magnetisation measured by the SQUID obtained after saturating the magnetisation at 400 K were fitted using a two-sublattice Weiss molecular mean field model of collinear ferrimagnetism described by the

system of non-linear equations

$$\begin{aligned} \mathbf{H}^{4a} &= n_W^{aa} \mathbf{M}^{4a} + n_W^{ac} \mathbf{M}^{4c} \\ \mathbf{H}^{4c} &= n_W^{ac} \mathbf{M}^{4a} + n_W^{cc} \mathbf{M}^{4c} \end{aligned} \quad (1)$$

where H^{4a} and H^{4c} are the internal sublattice molecular fields M^{4a} and M^{4c} are the magnetisations of the two sublattices, which are modelled by Brillouin functions and n_W^{aa} , n_W^{ac} and n_W^{cc} are the three Weiss coefficients. They are related to Heisenberg exchange constants \mathcal{J} by the expression

$$\mathcal{J}^{ij} = \frac{n_W^{ij} \rho \mu_0 (g \mu_B)^2}{Z^{ij}} \quad (2)$$

where ρ is the number of the Mn atoms on the i^{th} sublattice per unit cell volume, μ_0 is permeability of free space, g is the Landé g-factor for spin, μ_B is the Bohr magneton and Z is the coordination number, where $Z^{aa} = Z^{cc} = 12$ and $Z^{ac} = 8$ for $\text{Mn}_2\text{Ru}_x\text{Ga}$.

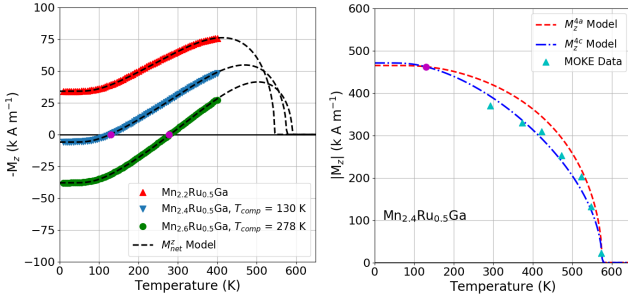


FIG. 9. (a) $\text{Mn}_{2.2}\text{Ru}_{0.5}\text{Ga}$, $\text{Mn}_{2.4}\text{Ru}_{0.5}\text{Ga}$ and $\text{Mn}_{2.6}\text{Ru}_{0.5}\text{Ga}$ thin films: Molecular field theory fit of net magnetisation versus temperature. (b) $\text{Mn}_{2.4}\text{Ru}_{0.5}\text{Ga}$: Calculated temperature dependences of Mn^{4a} and Mn^{4c} sublattice magnetisations compared with scaled MOKE data. The violet point marks compensation.

TABLE II. Summary of sublattice magnetisation at $T = 0$ K (M_0), spin angular momenta ($S^{4a,4c}$), Heisenberg exchange parameters from molecular field theory analysis of magnetisation data on the nine MRG thin films. The last column shows the ratio of the product of exchange constants with the coordination number $\mathcal{J}^{aa}Z^{aa} : \mathcal{J}^{ac}Z^{ac} : \mathcal{J}^{cc}Z^{cc}$.

Mn, Ru	S^{4a}	S^{4c}	M_0^{4c}	\mathcal{J}^{aa}	\mathcal{J}^{ac}	\mathcal{J}^{cc}	Ratio
y, x			(kA/m)	(K)	(K)	(K)	
2.2, 0.5	2.0	2.0	431	22.0	-24.5	11.6	10.0 : -7.4 : 5.3
2.4, 0.5	2.5	2.5	471	19.7	-20.2	10.3	10.0 : -6.8 : 5.3
2.6, 0.5	2.5	2.5	503	19.4	-20.1	9.6	10.0 : -6.9 : 5.0
2.0, 0.7	2.0	2.5	478	21.6	-20.5	10.4	10.0 : -6.3 : 4.8
2.2, 0.7	2.0	2.5	508	21.7	-19.7	10.5	10.0 : -6.1 : 4.8
2.4, 0.7	2.0	2.5	532	19.2	-16.1	10.0	10.0 : -5.6 : 5.2
1.8, 0.9	1.5	2.5	501	21.8	-23.2	7.0	10.0 : -7.1 : 3.2
2.0, 0.9	1.5	2.5	526	23.0	-23.8	7.2	10.0 : -6.9 : 3.1
2.2, 0.9	1.5	2.5	576	22.4	-20.6	6.2	10.0 : -6.4 : 2.8

When more than half the sites per formula unit are manganese, we assume the excess populates the $4d$ sites which are

symmetrically equivalent to the $4c$ sites. The $4a$ and $4b$ sites which accommodate Mn and Ga atoms are assumed to be fully occupied. The spin angular momentum quantum numbers for Mn atoms on each site, $S^{4a,4c}$, are multiples of $\frac{1}{2}$. The upper bound for $S^{4a,4c}$ is the sum of spins in a half-filled $3d$ orbital (5 spins). The lower bound is based on the Mn moment in similar compounds. (3 spins), so the quantum numbers in the Brillouin functions are chosen in the range $1.5 \leq S^{4a,4c} \leq 2.5$, and the sublattice magnetization is scaled to best represent the data. In metals, the spin moment per atom is rarely an integral number of Bohr magnetons and the sublattice moments at $T = 0$ K cannot be directly calculated from the $S^{4a,4c}$ quantum numbers appropriate for localised electrons due to orbital overlap and mixing. We found by density functional theory calculation that the Mn^{4a} sublattice moment at $T = 0$ K is nearly independent of Ru content for $0.5 \leq x \leq 1.0$ with a value of $m_0^{4a} = 2.70 \mu_B/\text{Mn}$, corresponding to a sublattice magnetisation $M_0^{4a} = 465 \text{ kA m}^{-1}$. [25] The net magnetisation at $T = 0$ K was extrapolated from the SQUID magnetometry data, shown in Fig. 5. Using this value, the magnetisation of the Mn^{4c} sublattice was inferred.

MOKE microscopy at a fixed wavelength ($\lambda = 632 \text{ nm}$) measures the Kerr rotation, which for MRG is essentially proportional to the magnetisation of the Mn^{4c} sublattice. Temperature-dependent MOKE data is compared with M_z of the Mn^{4c} sublattice calculated from the model in Fig. 9b, validating our approach. We use MOKE to determine T_C , since it covers the appropriate temperature range, and the Curie temperatures are then used as constraints in the fits. [31] The SQUID data, MFT fits and MOKE data for $x = 0.5$ thin films are all shown in Figs. 9a and 9b.

V. DISCUSSION

We define the Mn^{4c} moment as positive, coupled magnetically to the negative Mn^{4a} . In a previous study it was shown that well below T_C the Mn^{4a} moment is almost temperature independent whereas the Mn^{4c} moment varies nearly linearly as a function of temperature. [26] Therefore, adding (subtracting) atoms on the Mn^{4c} sublattice is expected to raise (lower) T_{comp} , whereas adding (subtracting) Mn atoms on the Mn^{4a} will increase (decrease) the sublattice moment, but since this moment is negative it results in a decrease (increase) of T_{comp} .

Increasing Ru raises T_{comp} [10] and within each Ru series increasing Mn also increases T_{comp} . Fig. 10a shows the relationship between T_{comp} and the number of valence electrons (n_v), with a slope of 530 K per electron. We conclude that the added Mn predominantly increases the Mn concentration on the $\text{Mn}^{4c/4d}$ sublattice. This is supported by the analysis of the densities of the thin films plotted in Fig. 4, which shows that there is no appreciable vacancy concentration for any composition in the series. Fig. 10b shows the linear relationship between m_0 and n_v with a slope of $1 \mu_B/\text{f.u.}$ per electron. The Slater-Pauling behaviour confirms the half-metallicity of all the MRG thin films.

The magnetometry data in Fig. 5, was recorded after magnetically saturating the samples perpendicular to their surface

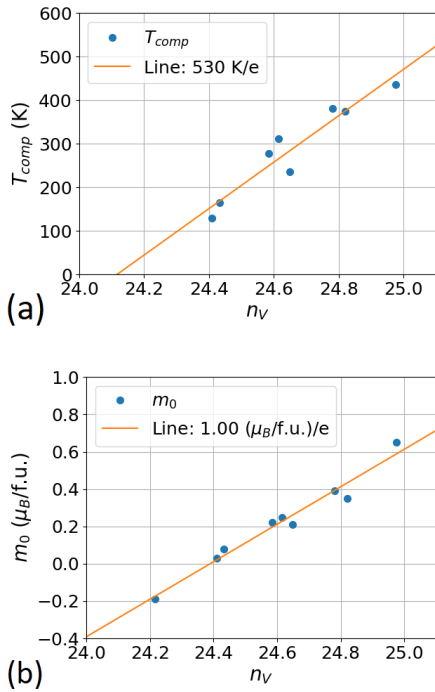


FIG. 10. (a) T_{comp} versus n_v : adding an electron (e) raises T_{comp} by 530 K. (b) m_0 versus n_v : adding an electron (e) raises m_0 by $1\mu_B/\text{f.u.}$ in agreement with the Slater-Pauling rule for a half-metal.

at $T = 400$ K. The z -projection of the net magnetisation was measured in zero field as a function of temperature during cool down. An ideal data set would include all three components of the sublattice specific moments which might be obtained using neutron diffraction or, if two components would suffice, by x-ray magnetic circular dichroism (XMCD). [32] Here we first discuss the magnetic mode of MRG first in the simplified model of two collinear sublattices, based on known variations of the Mn-Mn exchange parameters with the distance between interacting atoms.

Table II summarises the fit parameters for the series. For all compositions, the model agrees well with the magnetisation data measured along the easy axis, perpendicular to the film plane. The ratios of Heisenberg exchange constants are similar to those as reported previously for an MRG film with a comparable composition. [22] The main trend that emerges from the data is that as the Ru content of MRG increases, \mathcal{J}^{cc} decreases and while \mathcal{J}^{aa} and \mathcal{J}^{ac} remain almost constant. We explain the results as follows: \mathcal{J}^{aa} does not depend on Ru content because Mn^{4a} does not have much overlap with Ru^{4d} . When the number of Mn atoms in the unit cell exceeds 16 some Mn fills the $4d$ positions, giving rise to $\text{Mn}^{4c} - \text{Mn}^{4d}$ interactions, thereby the weakening \mathcal{J}^{cc} .

It is known that Mn-Mn distances in the range 250 pm - 280 pm generally lead to antiferromagnetic coupling that decreases in magnitude as the distance increases, whereas at distances greater than 290 pm the coupling becomes ferromagnetic. [33] In an unstrained Mn_2RuGa film, $a_0 = 598$ pm. The intra-sublattice distances between Mn atoms, where each site forms an fcc sublattice, are $a_0/\sqrt{2} \approx 423$ pm and the

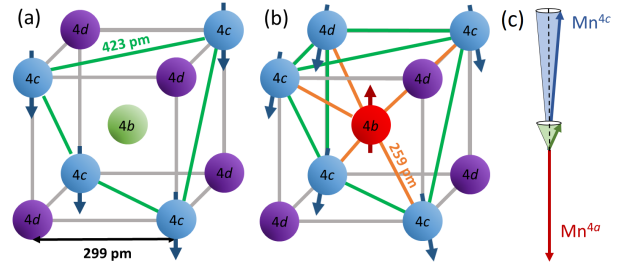


FIG. 11. Left: Inner cube (Mn^{4c} sublattice) in the cubic unit cell of the inverse Heusler structure XA (Fig. 1) showing the (a) $4c$ and $4d$ sites occupied by Mn atoms (blue with arrow) and Ru atoms (purple) with Ga (green) in the center, (b) one Ru atom is replaced with an Mn atom on a $4d$ site and Ga is replaced with Mn on the $4b$ site (red with arrow). Nearest neighbour ferromagnetic and antiferromagnetic couplings are represented by green and orange lines, respectively. The competition between exchange couplings can induce non-collinearity of sublattice moments locally. (c) Illustration of canting of net moment due to Mn^{4c} sublattice non-collinearity.

inter-sublattice $\text{Mn}^{4a} - \text{Mn}^{4c}$ or $\text{Mn}^{4b} - \text{Mn}^{4c}$ distance is $a_0\sqrt{3}/4 \approx 259$ pm, as indicated in Fig. 11. These distances correspond to ferromagnetic and antiferromagnetic exchange coupling, respectively. They are changed a little by the tetragonal distortion. Since the densities indicate that all sites are occupied, chemical disorder will arise in the unit cell. A first type of disorder arises from $\text{Mn}^{4a}\text{-Ga}^{4b}$ antisites and a second is the presence of Mn atoms on $4d$ sites. The Mn^{4c} sublattice portion of the unit cell is shown for Mn_2RuGa and $\text{Mn}_{2.25}\text{Ru}_{0.75}\text{Ga}$ in Figs. 11a and 11b, respectively, where the latter illustrates both types of disorder. The presence of Mn on $4d$ sites gives rise to FM coupling, marked with green lines in Fig. 11b. Changing the positions of Ga^{4b} and Mn^{4a} results in AFM coupling because the $\text{Mn}^{4b} - \text{Mn}^{4c}$ distance is ≈ 259 pm. This leads to random competing exchange on the Mn^{4c} sublattice, which will tend to give rise to a non-collinear spin structure. The local Mn^{4c} macroscopic sublattice moment may be expected to cant away from the anisotropy axis, forming an easy cone if four-fold in-plane anisotropy is negligible. The cone angle is the angle between the anisotropy axis and the moment. Local atomic environments differ on account of the random site occupancies that follow from the composition of the films, adding an element of randomness to the competing interactions, and the local canting angle.

In-plane applied field SQUID magnetometry data in Fig. 6, shows a component of the net moment which easily saturates along the *in-plane* field direction, unlike the hard component which normally extrapolates to the anisotropy field. For films with higher Ru content, which are closer to compensation at room temperature, the soft component dominates, and the determination of the anisotropy field is problematic. From the data on the first two samples in Fig. 6 we deduce a cone angle for the net moment of 21° . We have measured the cone angle in other MRG thin films by vector SQUID magnetometry and find values that can be as large as 40° . A feature of the *out-of-plane* loops in Fig. 6 is the step in magnetisation near remanence that corresponds to 40 % of the weak moment. We

associate this with a closing of the Mn^{4c} cone and a simultaneous opening of a cone on the Mn^{4a} sublattice, for which we have seen evidence in XMCD data. [32]

From the analysis of exchange energies and lattice parameters, it follows that sublattice non-collinearity results from competing positive and negative exchange coupling for the Mn^{4c} sublattice. This case has previously been argued for Mn^{2d} sites in tetragonal D0_{22} Mn_2RhSn . [34] A picture that represents our experimental observations well appears on the right hand side of Fig. 11c. We note that the Mn^{4c} cone angle needs to be only a few degrees to result in canting of the net moment by tens of degrees, because the net moment is more than an order of magnitude smaller than the sublattice moments, depending on how close the temperature is to compensation. The AHE loops in Fig. 6, where R_{xy} is proportional to the perpendicular component of the Mn^{4c} sublattice magnetisation, exhibit high remanence and we conclude that the very small in-plane moment of the Mn^{4c} sublattice cannot be detected.

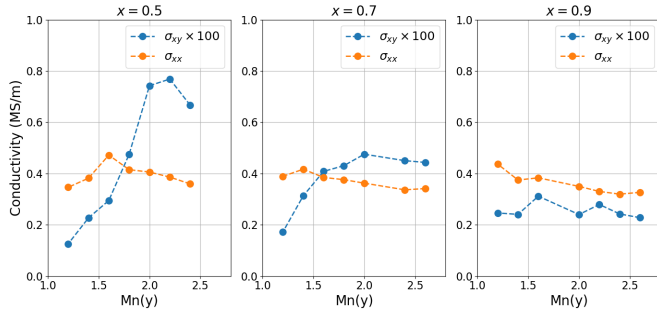


FIG. 12. Transverse (σ_{xy}) and longitudinal (σ_{xx}) conductivities of MRG thin films at 300 K for three Ru(x) series versus Mn(y) content. Note that σ_{xy} was calculated at magnetic saturation in $\mu_0 H = 1$ T at $T = 300$ K and in the data in the graph has been multiplied by a factor of 100.

The longitudinal (σ_{xx}) and transverse (σ_{xy}) conductivities of MRG thin films are plotted for three Ru(x) series versus Mn(y) in Fig. 12. The magnitude of σ_{xx} in the absence of a magnetic field is proportional to the conduction electron scattering. In all samples, σ_{xx} is almost constant whereas σ_{xy} shows a strong dependence on both Mn and Ru. To explain the observations, we need to consider the origins of AHE. There are two types of contributions to the anomalous conductivity. The first is the extrinsic contribution which is scattering dependent. There are two distinct mechanisms, skew scattering and side jump, where the former is proportional to σ_{xx} and the latter is independent of σ_{xx} . The second contribution is scattering independent (intrinsic) arising from Berry curvature and is independent of σ_{xx} . [30]

In Fig. 12, σ_{xy} exhibits a decrease with increasing Ru content. When Mn is varied with low x , σ_{xy} is seen to be independent of σ_{xx} , but for $x = 0.9$ σ_{xy} is approximately constant. The independence of σ_{xy} on σ_{xx} and its strong dependence on Ru content x suggests that for low x films the main contribution to AHE has an intrinsic origin. Impurity scattering, which depends on spin-orbit interaction, would be expected to increase with x . We find a maximal anomalous

Hall angle $\theta_{AH} = 2\%$ for $\text{Mn}_{2.2}\text{Ru}_{0.5}\text{Ga}$, which is ≈ 10 times higher than in conventional ferromagnets measured at 300 K. [35] Such large Hall angles are consistent with a large intrinsic contribution. While this could be a Berry phase effect, we are unable to disentangle the possible contributions of band structure (Weyl points), non-collinearity, Fermi surface effects and the influence of the incipient spin flop, which is expected for a ferrimagnet near compensation [36], and which is complete in $\text{Mn}_{2.2}\text{Ru}_{0.7}\text{Ga}$ at 7.65 T [32].

VI. CONCLUSIONS

At the outset $\text{Mn}_2\text{Ru}_{0.5}\text{Ga}$ was assumed to have vacancies on the $4d$ sites. Here we have shown from the observed densities that all four sites in MRG are all practically full, which implies that $\text{Mn}_2\text{Ru}_{0.5}\text{Ga}$ has 24 valence electrons, not 21 as originally thought. Full occupancy of the $4a$ and $4c$ sites by Mn leads to a collinear ferrimagnetic structure, which accounts for the magnetic material properties.

The substantial absence of vacancies implies the presence of chemical disorder. Specifically, the presence of some Mn on $4b$ and $4d$ sites promotes antiferromagnetic intra-sublattice exchange coupling on the Mn^{4c} sublattice, which leads to a non-collinear ferrimagnetic structure. The non-collinearity or the small net moment is much more pronounced than of the Mn^{4c} sublattice moment. The discrepancy between the AHE and measurements of magnetisation in Fig. 6 can therefore be explained. The independence of longitudinal and transverse conductivities indicates the dominance of the intrinsic contribution to AHE, which accounts for the large anomalous Hall angle observed in MRG films with low x . The reduction in spin polarisation with increasing Ru corresponds to a narrowing of the spin gap in the density of states. The half-metallicity of MRG in the range of compositions investigated is confirmed by Slater-Pauling behaviour of the net moment.

The magnetisation, spin polarisation and compensation point of MRG can be tuned to match the requirements of a specific application by varying the composition of the films. Highly crystalline, textured thin films with magnetic compensation ranging from $T = 0$ K up to the magnetic ordering temperature can be produced. The coercivity near compensation that can exceed 10 T, could permit the incorporation of single MRG layers in thin film stacks without any additional antiferromagnetic layers. [24]

ACKNOWLEDGMENTS

K.E.S. and J.M.D.C. acknowledge funding through Irish Research Council under Grant GOIPG /2016/308 and in part by the Science Foundation Ireland under Grants 12/RC/2278 and 16/IA/4534. G.A., A.J. R.S. S.L, J. O'B., P.S. and K.R. acknowledge funding from TRANSPiRE FET Open Programme, H2020. K.E. acknowledges funding from Science Foundation Ireland US-Ireland R&D (Center-to-Center)

under grant 16/USC2C/3287. N.T. was supported by the European Union's Horizon 2020 Research and Innovation

Programme under Marie Skłodowska-Curie EDGE Grant 713567, and in part by Science Foundation Ireland under grant 16/IA/4534.

-
- [1] D. Betto, K. Rode, N. Thiyagarajah, Y.-C. Lau, K. Borisov, G. Atcheson, M. Žic, T. Archer, P. Stamenov, and J. M. D. Coey, The zero-moment half metal: How could it change spin electronics?, *AIP Adv.* **6**, 055601 (2016).
- [2] J. Finley and L. Liu, Spintronics with compensated ferrimagnets, *Appl. Phys. Lett.* **116**, 110501 (2020).
- [3] T. Graf, C. Felser, and S. S. Parkin, Simple rules for the understanding of Heusler compounds, *Prog. Solid State Ch.* **39**, 1 (2011).
- [4] H. van Leuken and R. A. de Groot, Half-metallic antiferromagnets, *Phys. Rev. Lett.* **74**, 1171 (1995).
- [5] S. Wurmehl, H. C. Kandpal, G. H. Fecher, and C. Felser, Valence electron rules for prediction of half-metallic compensated-ferrimagnetic behaviour of Heusler compounds with complete spin polarization, *J. Phys. Cond. Mat.* **18**, 6171 (2006).
- [6] X. Hu, Half-metallic antiferromagnet as a prospective material for spintronics, *Adv. Mater.* **24**, 294 (2012).
- [7] I. Galanakis, P. Mavropoulos, and P. Dederichs, Electronic structure and Slater–Pauling behaviour in half-metallic Heusler alloys calculated from first principles, *J. Phys. D Appl. Phys.* **39**, 765 (2006).
- [8] P. Kharel, Y. Huh, N. Al-Aqtash, V. R. Shah, R. F. Sabirianov, R. Skomski, and D. J. Sellmyer, Structural and magnetic transitions in cubic Mn_3Ga , *J. Phys. Cond. Mat.* **26**, 126001 (2014).
- [9] M. Hakimi, M. Venkatesan, K. Rode, K. Ackland, and J. M. D. Coey, The zero-magnetization Heusler ferrimagnet, *J. Appl. Phys.* **113**, 17B101 (2013).
- [10] H. Kurt, K. Rode, P. Stamenov, M. Venkatesan, Y.-C. Lau, E. Fonda, and J. M. D. Coey, Cubic Mn_2Ga Thin Films: Crossing the Spin Gap with Ruthenium, *Phys. Rev. Lett.* **112**, 027201 (2014).
- [11] M. E. Jamer, Y. J. Wang, G. M. Stephen, I. J. McDonald, A. J. Grutter, G. E. Sterbinsky, D. A. Arena, J. A. Borchers, B. J. Kirby, L. H. Lewis, B. Barbiellini, A. Bansil, and D. Heiman, Compensated Ferrimagnetism in the Zero-Moment Heusler Alloy Mn_3Al , *Phys. Rev. Applied* **7**, 064036 (2017).
- [12] R. Stinshoff, G. H. Fecher, S. Chadov, A. K. Nayak, B. Balke, S. Ouardi, T. Nakamura, and C. Felser, Half-metallic compensated ferrimagnetism with a tunable compensation point over a wide temperature range in the Mn-Fe-V-Al Heusler system, *AIP Adv.* **7**, 105009 (2017).
- [13] N. Thiyagarajah, Y.-C. Lau, D. Betto, K. Borisov, J. M. D. Coey, P. Stamenov, and K. Rode, Giant spontaneous Hall effect in zero-moment Mn_2Ru_xGa , *Appl. Phys. Lett.* **106**, 122402 (2015).
- [14] K. E. Siewierska, N. Teichert, R. Schäfer, and J. M. D. Coey, Imaging Domains in a Zero-Moment Half Metal, *IEEE Trans. Mag.* **55**, 1 (2019).
- [15] N. Teichert, G. Atcheson, K. Siewierska, M. N. Sanz-Ortiz, M. Venkatesan, K. Rode, S. Felton, P. Stamenov, and J. M. D. Coey, Magnetic reversal and pinning in a perpendicular zero-moment half-metal, *Phys. Rev. Materials* **5**, 034408 (2021).
- [16] G. Bonfiglio, K. Rode, K. Siewierska, J. Besbas, G. Y. P. Atcheson, P. Stamenov, J. M. D. Coey, A. V. Kimel, T. Rasing, and A. Kirilyuk, Magnetization dynamics of the compensated ferrimagnet Mn_2Ru_xGa , *Phys. Rev. B* **100**, 104438 (2019).
- [17] S. Lenne, Y.-C. Lau, A. Jha, G. Y. P. Atcheson, R. E. Troncoso, A. Brataas, J. M. D. Coey, P. Stamenov, and K. Rode, Giant spin-orbit torque in a single ferrimagnetic metal layer, (2019), [arXiv:1903.04432 \[cond-mat.mes-hall\]](https://arxiv.org/abs/1903.04432).
- [18] M. Cubukcu, O. Boulle, M. Drouard, K. Garello, C. Onur Avci, I. Mihai Miron, J. Langer, B. Ocker, P. Gambardella, and G. Gaudin, Spin-orbit torque magnetization switching of a three-terminal perpendicular magnetic tunnel junction, *Applied Physics Letters* **104**, 042406 (2014).
- [19] L. Liu, O. J. Lee, T. J. Gudmundsen, D. C. Ralph, and R. A. Buhrman, Current-induced switching of perpendicularly magnetized magnetic layers using spin torque from the spin hall effect, *Phys. Rev. Lett.* **109**, 096602 (2012).
- [20] J. Finley, C.-H. Lee, P. Y. Huang, and L. Liu, Spin–Orbit Torque Switching in a Nearly Compensated Heusler Ferrimagnet, *Advanced Materials* **31**, 1805361 (2019).
- [21] C. Banerjee, N. Teichert, K. Siewierska, Z. Gercsi, G. Atcheson, P. Stamenov, K. Rode, J. M. D. Coey, and J. Besbas, Single pulse all-optical toggle switching of magnetization without gadolinium in the ferrimagnet Mn_2Ru_xGa , *Nat. Commun.* **11**, 4444 (2020).
- [22] C. S. Davies, G. Bonfiglio, K. Rode, J. Besbas, C. Banerjee, P. Stamenov, J. M. D. Coey, A. V. Kimel, and A. Kirilyuk, Exchange-driven all-optical magnetic switching in compensated 3d ferrimagnets, *Phys. Rev. Research* **2**, 032044(R) (2020).
- [23] C. Banerjee, K. Rode, G. Atcheson, S. Lenne, P. Stamenov, J. M. D. Coey, and J. Besbas, Ultrafast double pulse all-optical reswitching of a ferrimagnet, *Phys. Rev. Lett.*, Accepted (2021).
- [24] K. Borisov, D. Betto, Y. C. Lau, C. Fowley, A. Titova, N. Thiyagarajah, G. Atcheson, J. Lindner, A. M. Deac, J. M. D. Coey, P. Stamenov, and K. Rode, Tunnelling magnetoresistance of the half-metallic compensated ferrimagnet Mn_2Ru_xGa , *Appl. Phys. Lett.* **108**, 192407 (2016).
- [25] M. Žic, K. Rode, N. Thiyagarajah, Y.-C. Lau, D. Betto, J. M. D. Coey, S. Sanvito, K. J. O’Shea, C. A. Ferguson, D. A. MacLaren, and T. Archer, Designing a fully compensated half-metallic ferrimagnet, *Phys. Rev. B* **93**, 140202(R) (2016).
- [26] D. Betto, N. Thiyagarajah, Y.-C. Lau, C. Piamonteze, M.-A. Arrio, P. Stamenov, J. M. D. Coey, and K. Rode, Site-specific magnetism of half-metallic Mn_2Ru_xGa thin films determined by x-ray absorption spectroscopy, *Phys. Rev. B* **91**, 094410 (2015).
- [27] I. V. Soldatov and R. Schäfer, Advanced MOKE magnetometry in wide-field kerr-microscopy, *J. Appl. Phys.* **122**, 153906 (2017).
- [28] P. Stamenov, Point contact Andreev reflection from semimetallic bismuth - the roles of the minority carriers and the large spin-orbit coupling, *J. Appl. Phys.* **113**, 17C718 (2013).
- [29] K. Borisov, C.-Z. Chang, J. S. Moodera, and P. Stamenov, High Fermi-level spin polarization in the $(Bi_{1-x}Sb_x)_2Te_3$ family of topological insulators: A point contact Andreev reflection study, *Phys. Rev. B* **94**, 094415 (2016).
- [30] N. Nagaosa, J. Sinova, S. Onoda, A. H. MacDonald, and N. P. Ong, Anomalous Hall effect, *Rev. Mod. Phys.* **82**, 1539 (2010).

- [31] J. Smart, *Effective Field Theories of magnetism* (Saunders, London, 1966).
- [32] K. Siewierska, D. Betto, N. Teichert, G. Acheson, N. Brookes, and K. Rode, XMCD investigation of sublattice non-collinearity in compensated ferrimagnetic half-metallic thin films, Unpublished (2021).
- [33] J. M. D. Coey, *Magnetism and Magnetic Materials* (Cambridge University Press, Cambridge, 2010) Chap. Magnetic materials, pp. 395–396.
- [34] O. Meshcheriakova, S. Chadov, A. K. Nayak, U. K. Rößler, J. Kübler, G. André, A. A. Tsirlin, J. Kiss, S. Hausdorf, A. Kalache, W. Schnelle, M. Nicklas, and C. Felser, Large noncollinearity and spin reorientation in the novel Mn_2RhSn Heusler magnet, *Phys. Rev. Lett.* **113**, 087203 (2014).
- [35] T. Seki, S. Iihama, T. Taniguchi, and K. Takanashi, Large spin anomalous Hall effect in $\text{L1}_0\text{-FePt}$: Symmetry and magnetization switching, *Phys. Rev. B* **100**, 144427 (2019).
- [36] T. Fu, S. Li, X. Feng, Y. Cui, J. Yao, B. Wang, J. Cao, Z. Shi, D. Xue, and X. Fan, Complex anomalous Hall effect of CoGd alloy near the magnetization compensation temperature, *Phys. Rev. B* **103**, 064432 (2021).